

ND-A105 945

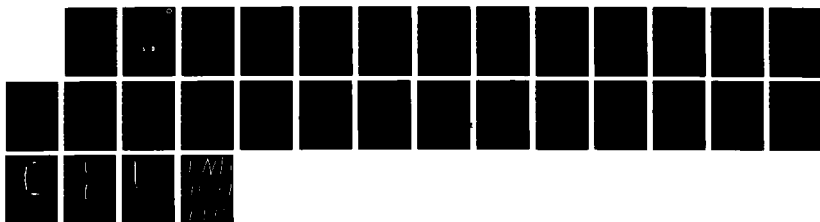
THE RAYLEIGH-TAYLOR INSTABILITY IN ABLATIVELY  
ACCELERATED TARGETS WITH 1 1. (U) NAVAL RESEARCH LAB  
WASHINGTON DC M H EMERY ET AL. 22 SEP 87 NRL-MR-6861

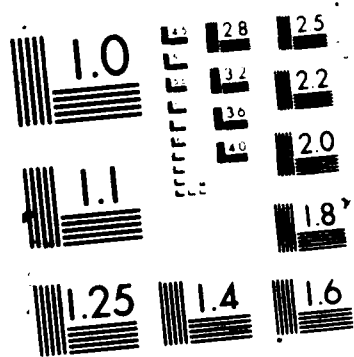
1/1

F/G 20/9

ML

UNCLASSIFIED





# Naval Research Laboratory

Washington, DC 20375-5000



NRL Memorandum Report 6061

DTIC FILE COPY

(2)

AD-A185 945

## The Rayleigh-Taylor Instability in Ablatively Accelerated Targets with 1, 1/2 and 1/4 $\mu$ m Laser Light

M. H. EMERY, J. P. DAHLBURG AND J. H. GARDNER

*Laboratory for Computational Physics and Fluid Dynamics*

September 22, 1987

DTIC  
ELECTED  
OCT 09 1987  
S D  
CD

A185 745

## REPORT DOCUMENTATION PAGE

1a. REPORT SECURITY CLASSIFICATION UNCLASSIFIED		1b. RESTRICTIVE MARKINGS													
2a. SECURITY CLASSIFICATION AUTHORITY		3. DISTRIBUTION/AVAILABILITY OF REPORT Approved for public release; distribution unlimited.													
2b. DECLASSIFICATION/DOWNGRADING SCHEDULE															
4. PERFORMING ORGANIZATION REPORT NUMBER(S) NRL Memorandum Report 6061		5. MONITORING ORGANIZATION REPORT NUMBER(S)													
6a. NAME OF PERFORMING ORGANIZATION Naval Research Laboratory	6b. OFFICE SYMBOL (If applicable) 4440	7a. NAME OF MONITORING ORGANIZATION Department of Energy													
6c. ADDRESS (City, State, and ZIP Code) Washington, DC 20375-5000		7b. ADDRESS (City, State, and ZIP Code) Washington, DC 20545													
8a. NAME OF FUNDING/SPONSORING ORGANIZATION Department of Energy	8b. OFFICE SYMBOL (If applicable)	9. PROCUREMENT INSTRUMENT IDENTIFICATION NUMBER													
8c. ADDRESS (City, State, and ZIP Code) Washington, DC 20545		10. SOURCE OF FUNDING NUMBERS PROGRAM ELEMENT NO.      PROJECT NO.      TASK NO.      WORK UNIT ACCESSION NO. 44-0859													
11. TITLE (Include Security Classification) The Rayleigh-Taylor Instability in Ablatively Accelerated Targets with 1, 1/2 and 1/4 $\mu$ m Laser Light															
12. PERSONAL AUTHOR(S) Emery, Mark H., Dahlburg, Jill P., Gardner, John H.															
13a. TYPE OF REPORT Interim	13b. TIME COVERED FROM 10/1/86 TO present	14. DATE OF REPORT (Year, Month, Day) 1987 September 22	15 PAGE COUNT 30												
16. SUPPLEMENTARY NOTATION															
17. COSATI CODES <table border="1"><tr><th>FIELD</th><th>GROUP</th><th>SUB-GROUP</th></tr><tr><td></td><td></td><td></td></tr><tr><td></td><td></td><td></td></tr><tr><td></td><td></td><td></td></tr></table>		FIELD	GROUP	SUB-GROUP										18. SUBJECT TERMS (Continue on reverse if necessary and identify by block number) Rayleigh-Taylor, Laser Ablation, Inertial Confinement Fusion Hydrodynamic Instabilities	
FIELD	GROUP	SUB-GROUP													
19. ABSTRACT (Continue on reverse if necessary and identify by block number)  We present the results of a series of detailed numerical simulations of the Rayleigh-Taylor instability in laser ablatively accelerated targets for a fairly wide range of initial conditions. It is shown that the Rayleigh-Taylor growth rate in an ablative environment is a strong function of the laser wavelength. For perturbation wavelengths about 3 times the inflight target thickness, the ratios of the numerical growth rates to the classical growth rates are of the order of 1/1.5, 1/2.5 and 1/3.5 for 1, 1/2 and 1/4 $\mu$ m laser light respectively. The numerical results are in good agreement with our theoretical model based on the ablative convection of vorticity away from the unstable ablation front. These results provide strong evidence for the viability of high-aspect-ratio shells in direct-drive laser fusion.															
20. DISTRIBUTION/AVAILABILITY OF ABSTRACT <input checked="" type="checkbox"/> UNCLASSIFIED/UNLIMITED <input type="checkbox"/> SAME AS RPT <input type="checkbox"/> DTIC USERS		21. ABSTRACT SECURITY CLASSIFICATION UNCLASSIFIED													
22a. NAME OF RESPONSIBLE INDIVIDUAL Mark H. Emery		22b. TELEPHONE (Include Area Code) (202) 767-3196	22c. OFFICE SYMBOL 4440												

## CONTENTS

I. INTRODUCTION .....	1
II. MODEL .....	3
III. NUMERICAL RESULTS .....	4
IV. THEORETICAL RESULTS .....	6
V. NONLINEAR RESULTS .....	10
VI. CONCLUSIONS .....	10
VII. ACKNOWLEDGEMENTS .....	11
REFERENCES .....	12

Accession For	
NTIS CRA&I	<input checked="" type="checkbox"/>
DMIC TAB	<input type="checkbox"/>
University Microfilms	<input type="checkbox"/>
Journal Issues	<input type="checkbox"/>
By	
Original	
Photocopy	
Photostat	
Microfilm	
Microfiche	
Other	
A-1	



## The Rayleigh-Taylor Instability in Ablatively Accelerated Targets with 1, 1/2 and 1/4 $\mu\text{m}$ Laser Light

### I. INTRODUCTION

The Rayleigh-Taylor<sup>1</sup> (RT) hydrodynamic instability can occur whenever a dense fluid is supported by a less dense fluid in a uniform gravitational field; or equivalently, a dense fluid is accelerated by a less dense fluid. Small perturbations at the interface between the two fluids grow exponentially in time as the denser fluid interchanges positions with the less dense fluid. This interchange process eventually leads to the formation of a nonlinear bubble-and-spike structure<sup>2</sup>.

In laser fusion, the cold, dense pellet is imploded by the rapid ablation of hot, low density plasma from the pellet's outer surface. This ablative acceleration process is Rayleigh-Taylor unstable. This desymmetrizing instability may grow at the ablation layer on the outer surface of the pellet, at an internal interface where materials of different density abut or at the fuel-pusher interface during the final deceleration phase of the implosion process: i.e., whenever the density and pressure gradients have opposite signs. The RT instability is a potential obstacle to laser fusion since it can cause shell fracture, fuel mix, or, in its mildest form, a nonuniform implosion that will reduce the convergence and severely diminish the energy gain of the fusion pellet. It is the ablative RT instability which we address in this report.

Classical, linear theory predicts that an initial perturbation,  $\eta_0$ , on the interface of an unstably stratified fluid in planar geometry will grow as  $\eta(t) = \eta_0 e^{\gamma t}$ , where  $\gamma = (Akg)^{1/2}$  with  $k = 2\pi/\lambda$ . Here  $\lambda$  is the wavelength of the perturbation,  $g$  is the acceleration,  $A = (\rho_u - \rho_l)/(\rho_u + \rho_l)$  is the Atwood number and  $\rho_u(\rho_l)$  is the density of the upper (lower) fluid. ( $A \sim 1$  in the laser-ablative case.) Recent theoretical<sup>3-10</sup>, numerical<sup>11-17</sup> and experimental<sup>18-20</sup> investigations of the RT instability in an ablative environment indicate that the growth behavior is quite different from the predictions of simple theory. Results from these investigations are in general agreement and indicate that the RT growth rate is about 1/2 of the classically predicted value for long wavelength perturbations with 1  $\mu\text{m}$  laser light and a strong cutoff occurs in the growth rate for short wavelength perturbations.

This reduction in the growth rate is important because it is the RT instability that ultimately dictates the allowed aspect ratio  $R/\Delta R$  (ratio of the distance pushed to the shell thickness) of the shell. The allowed aspect ratio both fixes the pressure required to drive the shell inward and indirectly determines the efficiency of the energy coupling between the laser and the shell<sup>21</sup>. If the RT instability grows at nearly its classically predicted rate then thick, low-aspect-ratio shells must be used. Such thick shells are predominantly undesirable for two reasons: they foster the growth of plasma instabilities, which scale as  $I\lambda_l^2$  (where  $I$  is the laser intensity and  $\lambda_l$  is the laser wavelength), and they lead to unacceptable low rocket efficiencies, in the range of 2% – 8%, with consequent relatively low pellet gains and high required driver energies for ignition<sup>22</sup>.

The allowed aspect ratio is a function of the RT growth rate and the wavelength of the most dangerous mode. In spherical coordinates, the planar classical growth rate  $(\text{kg})^{1/2}$  goes over to  $(l\ddot{R}/R)^{1/2}$ , for  $l \gg 1$ . Let us assume that the growth rate for the laser-ablative case is  $\epsilon (l\ddot{R}/R)^{1/2}$  where  $\epsilon \leq 1$ . If the shell is imploded halfway inward at constant acceleration then the number of  $e$ -foldings of unstable growth<sup>22</sup> is  $\gamma t = (\epsilon\pi/4)(2l)^{1/2}$ . Classical, incompressible theory suggests that the most dangerous mode is  $\lambda = \Delta R$ , the thickness of the shell; for this mode, the inner and outer surfaces are strongly coupled. However, numerical simulations have shown that when compressibility and nonlinear effects are taken into account, it is those perturbation wavelengths approximately 3 times the shell thickness that are most damaging to the implosion process<sup>16</sup>. For convenience, we set  $\lambda = 2\pi R_0/l \approx \pi\Delta R$ , and the limiting aspect ratio is given by  $R_0/\Delta R = (2\gamma t/\pi\epsilon)^2$ .

This limit can be quite severe since an initial aspect ratio of ten or so can become an in-flight aspect ratio (IFAR) of  $\sim 150$  as a result of compression. IFAR is defined as the inner radius of the target divided by the distance between the two radii where the density drops to  $1/e$  of the peak density. Consider a pellet polished so that after compression the largest surface perturbation has an amplitude of  $\sim 50 \text{ \AA}$ , and assume that the implosion process can survive about seven  $e$ -foldings of RT growth. This gives a final perturbation amplitude of  $\sim 5.5 \mu\text{m}$ , which would be  $\sim 1/4$  of the in-flight target thickness. If the RT instability grows at its classically predicted rate ( $\epsilon = 1$ ), then the maximum IFAR is limited to a value less than 20. The initial aspect ratio for this pellet would be about 1.5, and the laser intensity required to generate sufficient pressure to accelerate this shell to implosion velocities would be well above the threshold for plasma instabilities. These thick low-aspect-ratio shells would also severely limit the efficiency and gain of the fusion pellet<sup>21</sup>.

As noted above, there is general agreement that the RT growth rate is about  $1/2$  of the classically predicted value ( $\epsilon = 1/2$ ) with  $1\mu\text{m}$  laser light. This would permit an IFAR  $\sim 77$ , which is marginal at best. Recent results<sup>9,17</sup> have indicated that the RT growth rate is reduced to about 30% of the classical value with  $1/4\mu\text{m}$  laser light. With  $\epsilon = 0.30$ , the maximum IFAR  $\approx 220$ . These results imply that targets with an IFAR  $\sim 200$  can be stably imploded. Both the hydrodynamic efficiency and maximum laser intensity are strong functions of the IFAR<sup>22</sup>. With an IFAR of 200, efficiencies of greater than 15% are attainable with laser intensities of a few times  $10^{14} \text{ W/cm}^2$ . This further implies pellet gains greater than 200, which suggests that high-aspect-ratio shells are a viable design for direct-drive laser fusion.

It is the strong dependence of the RT growth rate on the laser wavelength which we address in this paper. Since the above analysis assumes perturbation wavelengths small compared to the target radius (large  $l$  numbers), we investigate the evolution of the RT instability in planar, laser ablatively accelerated targets. We present results from our FAST2D Laser-Matter-Interaction Code for a series of simulations which address the

issues of target thickness, perturbation wavelength, laser intensity and laser wavelength. The results are compared to our theoretical model where the inhibited growth is based on the ablative convection of vorticity away from the unstable ablation layer. In the next section we describe the numerical model we use to perform the simulations and discuss the initial conditions.

## II. MODEL

The evolution of the Rayleigh-Taylor instability in laser ablatively accelerated targets is modeled with our FAST2D Laser Matter Interaction Code. This is a fully two-dimensional, Cartesian, hydrodynamics code with a sliding Eulerian grid with variable grid spacing. The grid spacing is typically  $0.25 \mu m$  ( $0.125 \mu m$  for the high laser intensity cases) for 15 - 20 zones on either side of the ablation layer and increases uniformly to 2 -  $10 \mu m$  for most of the rest of the grid. The grids at the outer boundaries of the computational mesh are stretched to  $200 - 300 \mu m$ . The grid slides with the average velocity of the accelerated foil so that the ablation front remains approximately centered in the finely zoned region thus reducing convective errors.

FAST2D is fully Eulerian which is necessitated by the requirement to accurately model rotational flows. It should be pointed out that the flows stemming from the RT instability are inherently rotational. Vorticity is generated at the unstable ablation front by the baroclinic (noncollinear density and pressure gradients) nature of the profiles. The vorticity that arises from the differential twisting of the density and pressure surfaces feeds the "heavy" material into the spike and the "light" material into the bubble. Rectilinear Lagrangian algorithms cannot model rotational flows accurately without restructuring the grid which typically introduces an unacceptable amount of numerical diffusion.

The time-dependent equations for the continuity of mass, momentum and total energy are integrated numerically with sliding-zone flux-corrected- transport (FCT)<sup>23</sup>. FCT solves the continuity equations for the fluxes relative to moving zone boundaries. The overall scheme is second-order accurate and no artificial viscosity is explicitly required to maintain numerical stability. Mass, momentum and energy are both locally and globally conserved.

Thermal conduction is incorporated in a single-temperature model using a semi-implicit solution of the two-dimensional, classical, non-linear thermal conduction equation based on the model of Spitzer and Härn<sup>24</sup>. The laser energy is absorbed by classical inverse bremsstrahlung absorption with a resonant dump at the critical density. The laser light is at normal incidence. The fluid equations are closed with an ideal equation of state.

FAST2D and its counterpart in cylindrical geometry, FASTRZ, have been extensively compared with experimental results and have been found to give accurate results over a wide range of parameter space. These comparisons include scaling laws (mass ablation

rates, target velocities, velocities of ablated material and ablation pressures)<sup>25,26</sup>, velocity profiles of the ablated material<sup>27</sup>, target velocity asymmetries driven by imposed beam nonuniformities<sup>28</sup>, rear surface temperatures due to shock heating and thermal transport<sup>29</sup>, laser absorption rates and finite spotsize effects<sup>30</sup>, temperature and density profiles in the underdense ablated plasma<sup>31</sup> and the linear<sup>20</sup> and nonlinear<sup>19</sup> evolution of the RT instability in structured targets.

In order to obtain well defined RT growth rates we utilize a new "quiet start" method. FAST2D is run in a one-dimensional mode until a nearly steady-state distribution is attained. We start with a laser pulse which has a 2 ns HWHM (half-width-half-maximum) Gaussian rise after which the laser intensity is held constant at the peak value. A steady-state is typically reached  $\sim 2$  ns after the peak of the laser pulse. These steady-state profiles then serve as initial conditions in the two-dimensional model. At the start of each RT simulation, these steady-state density profiles are perturbed at the ablation front with a single wavelength perturbation. Small sinusoidal variations in the density are impressed in 10 zones on the high density side of the ablation layer. Initial perturbation strengths vary slightly and are bounded from above by a total mass perturbation of less than 0.5%. The growth rate of the instability is then measured during the constant intensity phase of the laser pulse during which time the target acceleration is approximately constant. This technique has several advantages: it avoids the mixing of RT phenomena and simple sound waves bouncing off the density perturbations; we are assured of having a self-consistent steady state profile which is difficult to obtain analytically with inverse bremsstrahlung absorption; and, we save computer time by using the same initial conditions for each perturbation wavelength, for fixed laser wavelength and intensity.

The computational growth rates are obtained by Fourier transformation of the summed mass of the foil. The mass of the foil ( $\rho R$ ) is integrated from the rear of the foil (the side away from the laser) to the ablation front for each transverse coordinate. A plot of the time evolution of the Fourier transform coefficients provides a very sensitive measure of the increase in areal mass nonuniformities due to the RT instability. Typically 5 - 7 e-foldings of exponential growth are obtained for the results presented here.

The foils used in this study are plastic (CH). The initial foil thicknesses are 55  $\mu m$  and 150  $\mu m$  with absorbed laser intensities of  $7 \times 10^{13} W/cm^2$  and  $3 \times 10^{14} W/cm^2$  respectively. The evolution of the RT instability on both targets is investigated with laser wavelengths of 1, 1/2 and 1/4  $\mu m$ . Perturbation wavelengths range from 5  $\mu m$  to 150  $\mu m$ . The numerical results are presented in the next section.

### III. NUMERICAL RESULTS

We first compare the evolution of the RT instability with and without the "quiet start" technique. The results are shown in Fig. 1. Here is plotted the log<sub>e</sub> of the amplitude of

the Fourier transform coefficient for the perturbed mode ( $\lambda = 20\mu m$ ) as a function of time for both cases. The initial target thickness is  $55\mu m$  with  $1\mu m$  laser light at  $7 \times 10^{13} W/cm^2$ . The square symbols are for the case where, starting from  $t = 0$ , the laser has a 2 ns Gaussian rise after which the intensity is held constant. There is an initial transition phase of approximately 0.75 ns duration while the flow patterns evolve into an eigenmode followed by rapid growth. After several oscillations, the growth finally evolves into a quasi-uniform exponential growth phase. The initial rapid oscillatory growth is most likely due to a combination of the strong shocks generated by the rising laser pulse and a non-self-consistent initial steady-state. The triangles are for the "quiet start" case and the  $t=0$  point is actually 4 ns after the laser is "turned on". The laser intensity is constant throughout the time plotted; and, after a slightly shorter transition period (0.50 ns) the growth is quite uniform. The growth rate is  $1.49 \times 10^9 ns^{-1}$ . The "quiet start" method is used for all the results presented here.

A comparison of the numerical growth rates (square symbols) to the classical growth rates (triangle symbols) as a function of perturbation wavelength for  $1\mu m$  laser light is shown in Fig. 2. Fig. 2a shows the results for  $55\mu m$  thick CH at  $7 \times 10^{13} W/cm^2$  and Fig. 2b is for  $150\mu m$  thick CH at  $3 \times 10^{14} W/cm^2$ . In both cases the computational growth rates follow an approximately  $k^{1/2}$  dependence with a moderately strong cutoff for perturbation wavelengths less than  $10\mu m$ . For perturbation wavelengths in the  $50\mu m$  range, the computational growth rate is reduced to  $\sim 75\%$  of the classical growth rate for the moderate intensity case ( $7 \times 10^{13} W/cm^2$ ) and to  $\sim 65\%$  of classical for the high intensity case ( $3 \times 10^{14} W/cm^2$ ). The classical growth rate is given by  $(kg)^{1/2}$  where  $g = P_a/M$ .  $P_a$  is the average ablation pressure across the foil surface and  $M$  is the mass density of the foil. For the moderate intensity case  $P_a = 8.9 Mb$  and  $M = 4.94 \times 10^{-3} gm/cm^2$  and thus  $g = 1.8 \times 10^{15} cm/s^2$ . For the high intensity case  $P_a = 24.5 Mb$  with  $M = 1.23 \times 10^{-2} gm/cm^2$  and  $g = 2.0 \times 10^{15} cm/s^2$ . In each case there were only slight variations in  $g$ ,  $O(\pm 1\%)$ , as the perturbation wavelength was varied.

The results with  $1/2\mu m$  laser light are shown in Fig. 3. Again, the moderate intensity comparison is in Fig. 3a and the high intensity comparison is in Fig. 3b. In both cases the computational growth rates are more strongly inhibited than in the  $1\mu m$  case and the dependence on the perturbation wavelength is reduced. The short perturbation wavelength cutoff is not as dominant as in the  $1\mu m$  case or it occurs at wavelengths less than  $5\mu m$ . The growth rate is reduced to 50% (45%) of classical for the moderate (high) intensity case for wavelengths  $O(50\mu m)$ . The parameters are  $P_a = 10 Mb$ ,  $M = 5.0 \times 10^{-3} gm/cm^2$  and  $g = 2.0 \times 10^{15} cm/s^2$  for the moderate intensity case; and,  $P_a = 30.5 Mb$ ,  $M = 1.27 \times 10^{-2} gm/cm^2$  and  $g = 2.4 \times 10^{15} cm/s^2$  for the high intensity case.

The RT growth rates are even more strongly inhibited with  $1/4\mu m$  laser light as shown in Fig. 4. The RT growth rate is strongly reduced for both the moderate (Fig. 4a) and high (Fig. 4b) intensity cases and the dependence on the perturbation wavelength is

strongly suppressed. For  $\lambda \sim 50 \mu m$ , the growth rate is only 30% of the classical value. For the moderate intensity case,  $P_a = 15.5 \text{ Mb}$ ,  $M = 4.8 \times 10^{-3} \text{ gm/cm}^2$  and  $g = 3.2 \times 10^{15} \text{ cm/s}^2$ ; and, for the high intensity case,  $P_a = 40.6 \text{ Mb}$ ,  $M = 1.25 \times 10^{-2} \text{ gm/cm}^2$  and  $g = 3.25 \times 10^{15} \text{ cm/s}^2$ .

These results are summarized are Fig. 5 where the ratios of the numerical growth rates to the classical growth rates are plotted as a function of the perturbation wavelength and the laser wavelength for both the moderate (Fig. 5a) and high (Fig. 5b) intensity laser cases. It is quite clear that the RT growth rate is strongly dependent upon the laser wavelength. With the exception of the  $1 \mu m$  results, there appears to be little dependence upon the laser intensity. Resonant absorption is more dominant with  $1 \mu m$  laser light and this may be influencing the results. This is addressed in more detail in the next section. The results indicate that the growth rate reduction may be asymptoting to a constant reduction factor for the very long wavelength modes; see Fig. 5b. The reduction factors are  $1/1.54$ ,  $1/1.82$  and  $1/3$  for the very long wavelength perturbations for  $1$ ,  $1/2$  and  $1/4 \mu m$  laser light respectively. In the next section the theoretical model is summarized and compared to the numerical results.

#### IV. THEORETICAL RESULTS

There have been many theoretical models developed over the past several years in an attempt to explain the inhibited RT growth in ablative accelerated targets. These models have proposed convection<sup>3</sup>, mass ablation<sup>5,6,9</sup>, thermal conduction<sup>3,5</sup>, compressibility<sup>4,6</sup>, combinations of the above<sup>6</sup> and density gradient stabilization<sup>7</sup> as the cause of the inhibited growth. Recently it has been shown that compressibility plays a minor role<sup>4,8</sup> and can, in fact, be destabilizing<sup>8</sup>. In direct-drive laser fusion the density-gradient scalelengths are too small to significantly reduce the RT growth rate by density-gradient stabilization<sup>17</sup>. Fig. 6 compares the steady-state density and pressure profiles for both the  $1 \mu m$ , at  $10^{13} \text{ W/cm}^2$ , and  $1/4 \mu m$ , at  $3 \times 10^{14} \text{ W/cm}^2$ , cases. The density-gradient scalelengths are  $0.49$  and  $0.40 \mu m$  respectively and in neither case would the density gradients provide a significant reduction in the growth rate.

The vorticity generated by the noncollinear nature of the density and pressure profiles is the controlling element in the evolution of the RT instability<sup>17</sup>. In particular it is the ablative convection of vorticity away from the unstable ablation layer that reduces the rate at which the fluids are interchanged. The details of the analytic scheme will be published elsewhere<sup>32</sup> and we will only summarize the results here.

We consider the oscillations of an inviscid, thin layer of fluid (of thickness,  $h$ ) with an exponential density gradient bounded on both sides by inviscid fluids of constant density of semi-infinite extent. In this two-dimensional geometry, the equation describing the time

evolution of the vorticity of the thin layer is obtained by taking the curl of the equation of motion and is given by

$$\dot{\vec{\omega}} = \nabla \rho \times \nabla p / \rho^2 - \vec{V} \cdot \nabla \vec{\omega} - \vec{\omega} (\nabla \cdot \vec{V}), \quad (IV - 1)$$

where  $\rho$  is the density and  $p$  is the pressure. The first term on the RHS is the baroclinic source term which will generate vorticity whenever the density and pressure gradients are noncollinear. See Fig. 6. The region between the density peak and the pressure peak is the RT unstable region<sup>33</sup>. The second and third terms are the convective and compressible terms respectively.

We first consider the incompressible, non-ablative case and perform a first order perturbation expansion on the above equation. Expressing the perturbed velocities in terms of the stream function and evaluating the boundary conditions, the growth rate for the interfacial mode takes the form

$$\gamma^2 / kg = \frac{[AL + kh(AL + 2)]}{2(L + Akh)} [1 + [1 - \frac{4kh(L + Akh)(A + L)}{[AL + kh(AL + 2)]^2}]^{1/2}], \quad (IV - 2)$$

where  $A = (\rho_u - \rho_l)/(\rho_u + \rho_l)$  is the Atwood number with  $L = \ln(\rho_u/\rho_l)$  and  $\rho_u(\rho_l)$  is the density of the upper (lower) fluid,  $\rho_u = \rho_l e^{h/H}$ . Eq. (IV-2) can be simplified by setting  $L = h/H$ , and for  $kh$  small

$$\gamma^2 / kg \approx A(1 + kh)(1 - kh/A^2), \text{ or}$$

$$\gamma^2 / kg \approx 1/(1 + k^2 h^2), \quad (IV - 3)$$

for  $A \rightarrow 1$ . The mode is unstable if  $\rho_u \geq \rho_l$  and the intermediate layer reduces the growth rate from the classical value. The classical value is recovered in the limit  $kh \rightarrow 0$ . In the typical laser ablative accelerated target, the thickness of the ablation region is quite small,  $h \sim O(1-2 \mu m)$  (see Fig. 6), and there will be little reduction in the growth rate except for very short wavelength perturbations.

To account for the ablative convection of vorticity away from the unstable layer, we incorporate an exponentially varying, zeroth-order ablation velocity ( $\vec{V}_a$ ) which satisfies the steady-state continuity equation,  $\nabla \cdot (\rho \vec{V}_a) = 0$ . Assuming incompressible perturbations,

we obtain a fifth order dispersion relation. In the limit  $kh \rightarrow 0$ , this reduces to a quadratic and the growth rate for the infinitesimally thin layer, ablative RT case is

$$\gamma = [(\frac{AkV_a}{2})^2 + \gamma_0^2]^{1/2} - \frac{AkV_a}{2} \quad IV-4$$

where  $\gamma_0 = (Ak^2g)^{1/2}$  is the classical result. This expression is similar those in Ref. 3 and 6 except that Ref. 3 uses the target velocity (and thus little stabilization) and Ref. 6 invokes supersonic flow.

If the ablation velocity is large, Eq. IV-4 predicts strongly inhibited growth of the instability; the difficulty is in what to choose for the ablation velocity. Figure 7 shows the isovorticity contours on the target surface early in the evolution of the  $20 \mu\text{m}$  RT instability for  $1/4 \mu\text{m}$ ,  $7 \times 10^{13} \text{ W/cm}^2$  laser light on a  $55 \mu\text{m}$  thick plastic target. The laser light is impinging on the target from the right. The ablation velocity ( $V_a$ , cm/s), which is convecting vorticity away from the target surface, is plotted on top of the vorticity contours. In order to compare the above theoretical expression with the numerical growth rates, the ablation velocities are taken from the numerical simulations and are measured at the center of the unstable shear layer on the ablation front.

The theoretical growth rates (solid circles) are compared to the numerical growth rates in Figures 2-4. The agreement is quite good for the long wavelength modes. The lack of agreement at the short wavelength perturbations, especially for  $1 \mu\text{m}$  laser light, is due to the assumption of an infinitely thin vortex sheet at the ablation front. Eq. IV-4 cannot reproduce the short wavelength cutoff. In order to account for the finite size nature of the unstable layer, we replace the classical expression in Eq. IV-4 ( $\gamma_0$ ) by the approximate expression for the growth rate for an exponential density layer of finite thickness (Eq. IV-3). These results are shown as the open circular symbols in Figs. 2-4. This modification to Eq. IV-4 has little effect on the long wavelength modes and does a reasonable job of reproducing the short wavelength cutoff.  $h$  is taken to be the distance between the density peak and the pressure peak as determined from the steady-state profiles. The size of  $h$  is laser intensity dependent;  $h = 1.0 \mu\text{m}$  for the moderate intensity case and  $0.75 \mu\text{m}$  for the high intensity case.

The strong reduction in RT growth with short wavelength lasers is due to the increase in ablation velocity as the laser wavelength is reduced. The higher mass ablation rate for short wavelength lasers produces a higher acceleration of plasma away from the ablation surface and therefore a larger value of  $V_a$ . Figure 8 is a plot of the ablation velocity ( $V_a$ ) obtained from the FAST2D Model as a function of distance from the target surface for  $1/2$  and  $1/4 \mu\text{m}$  laser light. All the calculations were with a  $55 \mu\text{m}$  thick CH target with an absorbed intensity of  $7 \times 10^{13} \text{ W/cm}^2$  under nearly steady-state conditions. Note that at the center of the unstable shear layer, the ablation velocity for  $1/4 \mu\text{m}$  light is over

three times larger than for  $1 \mu\text{m}$  light. These results are substantiated by simple scaling arguments<sup>17</sup> which show that  $V_a \propto \lambda^{-1}$ . The growth rate for the RT instability will be more strongly inhibited with short wavelength lasers than with  $1 \mu\text{m}$  laser light, since the vorticity will be convected away at a faster rate. Of course, at large distances from the ablation layer the blowoff velocity is less for shorter wavelength lasers.

It is somewhat difficult to obtain a definitive scaling relationship between the ablation velocity and the laser wavelength and intensity. This is because of the dependence of the thickness of the unstable layer on the laser intensity and the strongly exponential nature of the ablation velocity. For low intensity lasers,  $\sim 10^{13} \text{ W/cm}^2$ , the distance between the density peak and pressure peak is  $\sim 1.5 \mu\text{m}$  and the center of the vortex layer is nearly  $2 \mu\text{m}$  from the density peak (see Ref. 16). As a result, at this low intensity, the ablation velocity through the vortex sheet is quite large,  $> 10^6 \text{ cm/s}$ . For the moderate and high intensity cases simulated here, the distance between the density and pressure peaks is  $1 \mu\text{m}$  or less, and the center of the unstable layer is about a micron from the density peak. This results in an ablation velocity through the vortex layer of less than  $10^6 \text{ cm/s}$  for  $1 \mu\text{m}$  light at  $7 \times 10^{13} \text{ W/cm}^2$ . Note however, at comparable distances ( $\sim 2 \mu\text{m}$ ), the ablation velocity is greater than that for  $10^{13} \text{ W/cm}^2$ . Further work is in progress to investigate this ablation layer scaling.

Recent work by Takabe, et al.<sup>9</sup> also showed an enhanced reduction in the RT growth rate with  $1/4 \mu\text{m}$  laser light. There they applied an eigenvalue analysis to the linearized equations for stationary ablating plasmas. Their results agreed well with ours<sup>13</sup> and those of McCrory et al.<sup>12</sup> for  $1 \mu\text{m}$  laser light. The growth rates they obtained with  $1/4 \mu\text{m}$  light were factors of 2-3 smaller than the rates obtained with the FAST2D Model. The most likely source of this discrepancy is due to their assumption that all of the laser light is absorbed at the critical density. We find in the numerical simulation that most of the laser energy is absorbed through inverse bremsstrahlung with  $1/4 \mu\text{m}$  light and thus the temperature profile is not nearly so steep as that resulting from resonant absorption. As a result, the mass ablation rate with inverse bremsstrahlung absorption is not as large as one would expect from scaling laws based on energy deposition at critical density and the growth rate is not reduced by as large a factor.

To test this hypothesis, we ran FAST2D with 100% deposition at critical for  $1/4 \mu\text{m}$ ,  $3 \times 10^{14} \text{ W/cm}^2$  laser light on a  $150 \mu\text{m}$  thick CH target. Under these conditions, the ratio of numerical to classical growth rate is 0.2 which is 2/3 of the growth rate obtained with inverse bremsstrahlung absorption. The analytical expression obtained by Takabe et al. is based on the initial target mass. If this is modified to accommodate the accelerated target mass, which is  $\sim 80\%$  of the initial target mass, their growth rates would increase by 10-15 % and would be in good agreement with our resonant absorption results. We believe that these two effects explain the very strong reduction in growth rates with  $1/4 \mu\text{m}$  laser light obtained by Takabe, et al.<sup>9</sup>

## V. NONLINEAR RESULTS

As corrugations on the interface of an unstably stratified fluid grow in amplitude, they eventually form the nonlinear bubble-and-spike structure<sup>2</sup>. The spikes are characterized by thin sheets (in 2 dimensions) of dense fluid which "fall" and the bubbles are rounded regions of light fluid which "rise". When the amplitude of the spike becomes large,  $O(\lambda/2)$ , the spike partially shields the bubble from the ablation process and the vorticity is advected down the sides of the spike causing a Kelvin-Helmholtz-like (KH) rollup of the spike tips. We have previously reported on this phenomena with low intensity laser light<sup>12,15</sup>. We find a somewhat similar process occurring with high intensity lasers.

Figure 9a shows the isodensity contours after  $\sim 4$  e-foldings of growth for  $1/4 \mu\text{m}$  light at  $7 \times 10^{13} \text{ W/cm}^2$ . The wavelength of the perturbation is  $20 \mu\text{m}$ . At this time the spike region is still quite broad and the bubble region is relatively flat. The corresponding streamlines are plotted in Figure 9b. Note the strong vertical flow at the base of the spike. The flow pattern (in a case for which all the fluid flow is from left to right) is quite similar to the vortex ring that is formed when fluid emanates from a nozzle. Figure 10 shows the isodensity contours at a slightly later time. The bubble is now rounded and the spike is much narrower with significant broadening of the spike tip.

Figures 11 and 12 illustrate the nonlinear bubble-and-spike structure for  $1/2 \mu\text{m}$ ,  $7 \times 10^{13}$  and  $1 \mu\text{m}$ ,  $3 \times 10^{14}$  laser light respectively. Although all the above cases indicate some degree of KH-like rollup of the spike tips, the degree of rollup is not as large as that obtained for low intensity laser light and the bubble region remains quite flat. This is due to the higher mass ablation rate with the higher intensity and/or shorter wavelength lasers. This is more in agreement with the work of McCrory et al.<sup>12</sup> and Verdon et al.<sup>14</sup> than was our previous lower intensity case<sup>13</sup>. Note that even with the relatively large spike amplitude, the bulk of the target is still flat and is uniformly accelerated.

## VI. CONCLUSIONS

We have shown, through a series of detailed numerical simulations, that the Rayleigh-Taylor growth rate for laser ablatively accelerated targets is a strong function of laser wavelength. The numerical results agree well with the theoretical model based on the convection of vorticity away from the unstable ablation front. As the laser wavelength is reduced, the ablation velocity increases thereby convecting vorticity away at a faster rate and reducing the rate at which the fluids are interchanged.

If we consider perturbation wavelengths of  $\sim 60 \mu\text{m}$ , the RT growth rate is reduced by factors of  $1/1.54$ ,  $1/2.22$  and  $1/3.33$  for  $1$ ,  $1/2$  and  $1/4 \mu\text{m}$  laser light respectively. Assuming the shell can survive up to 7 e-foldings of exponential growth at this perturbation wavelength, the maximum in-flight aspect ratio for a reactor size pellet is  $R/\Delta R \approx 47$ .

98 and 220 for 1, 1/2 and 1/4  $\mu\text{m}$  laser light. It has been shown<sup>22</sup> that with an IFAR of 200, efficiencies of greater than 15% are attainable with 1/4  $\mu\text{m}$  light and intensities of a few times  $10^{14}$  W/cm<sup>2</sup>. The results presented here imply that targets with an initial aspect ratio of  $\sim 10$  and an IFAR  $\sim 200$  can be stably imploded. This suggests that moderately high-aspect-ratio shells are a viable design for direct-drive laser fusion with short wavelength (1/4  $\mu\text{m}$ ) laser light.

It is clear that ablation layer phenomena dominates the development and evolution of the RT instability in laser ablatively accelerated targets. The convection velocity at the ablation front controls the degree of inhibition of the RT growth. The thickness of the ablation front strongly influences the cutoff at short perturbation wavelengths. More work is needed in this area, to develop scaling relationships for ablation layer parameters as a function of laser wavelength and intensity and target composition, all under inverse bremsstrahlung absorption conditions. We also need additional experimental data on the RT instability to test these predictions.

## VII. ACKNOWLEDGEMENTS

We thank S. E. Bodner for urging that we study the laser wavelength dependence of the Rayleigh-Taylor instability and for various interesting discussions during the course of this work. This work was supported by the U. S. Department of Energy and the Office of Naval Research.

## REFERENCES

1. Lord Rayleigh, *Theory of Sound*, 2nd. ed. (Dover, New York, 1894), Vol. 2; G. I. Taylor, Proc. R. Soc. London Ser. A 201, 192(1950).
2. H. Helmholtz, Philos. Mag. Ser. 4, 36, 337(1868); Lord Kelvin, *Hydrodynamics and General Dynamics* (Cambridge University, Cambridge, 1910), p. 69ff.
3. S. E. Bodner, Phys. Rev. Lett. 33, 761(1964).
4. L. Baker, Phys. Fluids 26, 950(1983).
5. H. Murakami, T. Yabe and K. Niu, Trans. Jpn. Soc. Aero. Space Sci. 20, 100(1977).
6. W. M. Manheimer and D. G. Colombant, Phys Fluids 27, 983(1984).
7. K. O. Mikaelian and J. D. Lindl, Phys. Rev A 29, 290(1984).
8. I. B. Bernstein and D. L. Book, Phys. Fluids 26, 453(1983).
9. H. Takabe, K. Mima, L. Montierth and R. L. Morse, Phys. Fluids 28, 3676(1985).
10. H. J. Kull and S. I. Anisimov, Phys. Fluids 29, 2067(1986).
11. J. D. Lindl and W. C. Mead, Phys. Rev. Lett. 34, 1273(1975).
12. R. L. McCrory, L. Montierth, R. L. Morse and C. P. Verdon, Phys. Rev. Lett. 46, 336(1981).
13. M. H. Emery, J. H. Gardner and Jay P. Boris, Phys. Rev. Lett. 48, 677(1982), and Phys. Rev. Lett. 56, 1757(E) (1986).
14. C. P. Verdon, R. L. McCrory, R. L. Morse, G. R. Baker, D. I. Meiron and S. A. Orszag, Phys. Fluids 25, 1653(1982).
15. R. G. Evans, A. J. Bennet and G. J. Pert, Phys. Rev. Lett. 49, 1639(1982).
16. M. H. Emery, J. H. Gardner and J. P. Boris, Appl. Phys. Lett. 41, 808(1982), and Appl. Phys. Lett. 48, 1406(E) (1986).
17. M. H. Emery, J. H. Gardner and S. E. Bodner, Phys. Rev. Lett. 57, 703(1986).

18. A. J. Cole, J. D. Kilkenny, C. J. Hooker and P. T. Rumsby, *Nature (London)* **299**, 329(1982).
19. R. R. Whitlock, M. H. Emery, J. A. Stamper, E. A. McLean, S. P. Obenschain and M. C. Peckerar, *Phys. Rev. Lett.* **52**, 819(1984).
20. J. Grun, M. H. Emery, S. Kacenjar, C. B. Opal, E. A. McLean, S. P. Obenschain, B. H. Ripin and A. Schmitt, *Phys. Rev Lett.* **53**, 1352(1984).
21. S. E. Bodner, *J. Fusion Energy* **1**, 221(1981).
22. J. H. Gardner and S. E. Bodner, *Phys. Fluids* **26**, 72(1986).
23. J. P. Boris and D. L. Book, *Methods Comput. Phys.* **16**, 85(1976).
24. L. Spitzer and R. Härm, *Phys. Rev.* **89**, 977(1953).
25. The Laboratory for Computational Physics and The Plasma Physics Division, Naval Research Laboratory Memorandum Report No. 4369, November 1980; R. Decoste, S. E. Bodner, B. H. Ripin, E. A. McLean, S. P. Obenschain and C. M. Armstrong, *Phys. Rev. Lett.* **42**, 1673(1979).
26. J. H. Gardner and S. E. Bodner, *Phys. Rev. Lett.* **47**, 1137(1981).
27. M. J. Herbst, P. G. Burkhalter, D. Dustin, M. Emery, J. Gardner, J. Grun, S. P. Obenschain, B. H. Ripin, R. R. Whitlock, J. P. Apruzese and J. Davis, *Laser Int. and Rel. Plasma Phenomena*, ed. by H. Hora and G. Miley (Plenum, New York, 1984) Vol. 6, p. 317.
28. M. H. Emery, J. H. Orens, J. H. Gardner and J. P. Boris, *Phys. Rev. Lett.* **48**, 253(1982).
29. E. A. McLean, J. A. Stamper, J. Grun, C. K. Manka, H. R. Griem, S. P. Obenschain, B. H. Ripin, S. E. Bodner, M. H. Emery, J. H. Gardner, T. N. Lee, A. N. Mostovych, K. J. Kearney, *Bull. Am. Phys. Soc.* **31**, 1410(1986).
30. J. H. Gardner, M. J. Herbst, F. C. Young, J. A. Stamper, S. P. Obenschain, C. K. Manka, K. J. Kearney, J. Grun, D. Dustin and P. G. Burkhalter, *Phys. Fluids* **29**, 1305(1986).
31. P. G. Burkhalter, M. J. Herbst, D. Dustin, J. Gardner, M. Emery, R. R. Whitlock, J. Grun, J. P. Apruzese and J. Davis, *Phys. Fluids* **26**, 3650(1983).

32. M. H. Emery and J. H. Gardner, 15th Annual Anomalous Absorption Conf., June, 1985 (Banff, Alberta) to be sub. to Phys. Fluids.

33. Yu. F. Afanas'ev, N. G. Basov, E. G. Gamalii, O. N. Krokhin and V. B. Rozanov, Pis'ma Zh. Eksp. Teor. Fiz. **23**, 617(1976), ( JETP Lett. **23**, 566(1976) ).

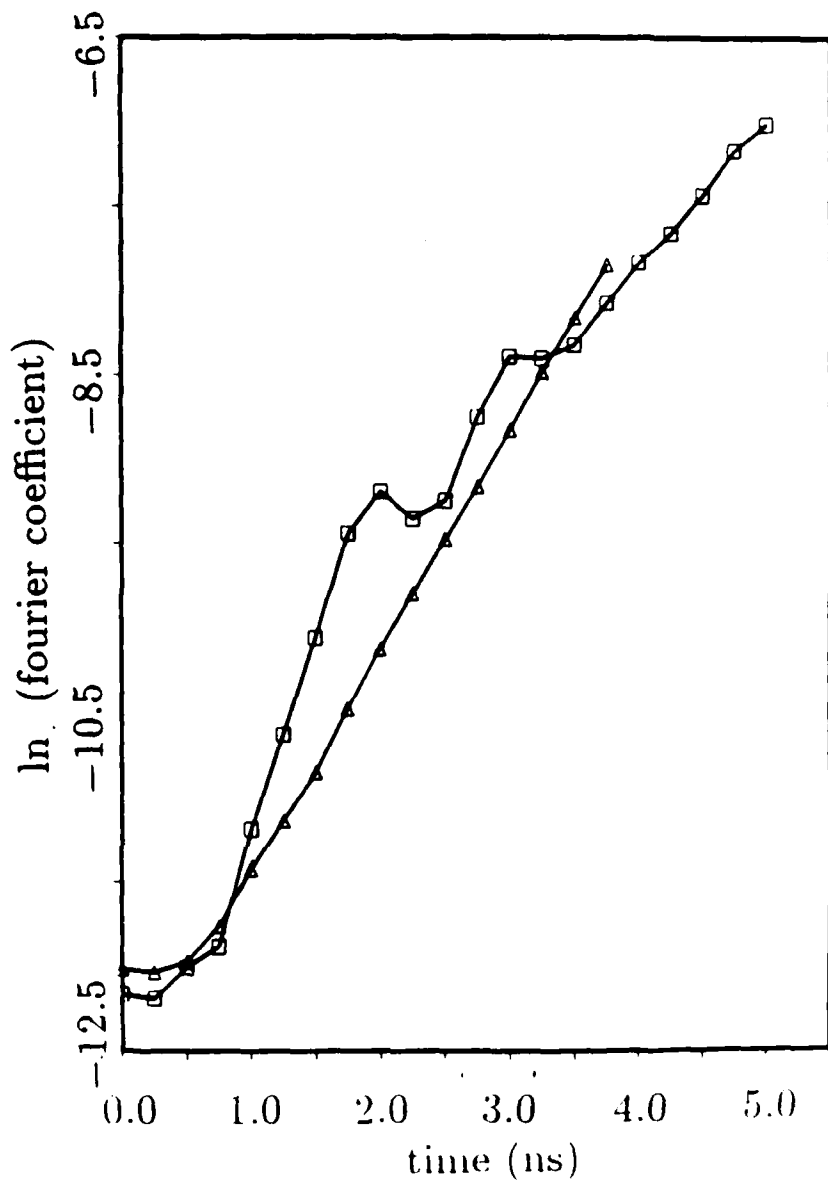


Fig.1. Plot of the log<sub>e</sub> of the Fourier transform coefficient of the Rayleigh-Taylor unstable mode as a function of time for both the nonsteady-state (squares, temporally rising laser pulse) and steady-state (triangles, "quiet start", constant laser pulse) initial conditions. In both cases the initial target thickness was 55  $\mu\text{m}$  with 1  $\mu\text{m}$  laser light with a peak intensity of  $7 \times 10^{13} \text{ W/cm}^2$  and a perturbation wavelength of 20  $\mu\text{m}$ .

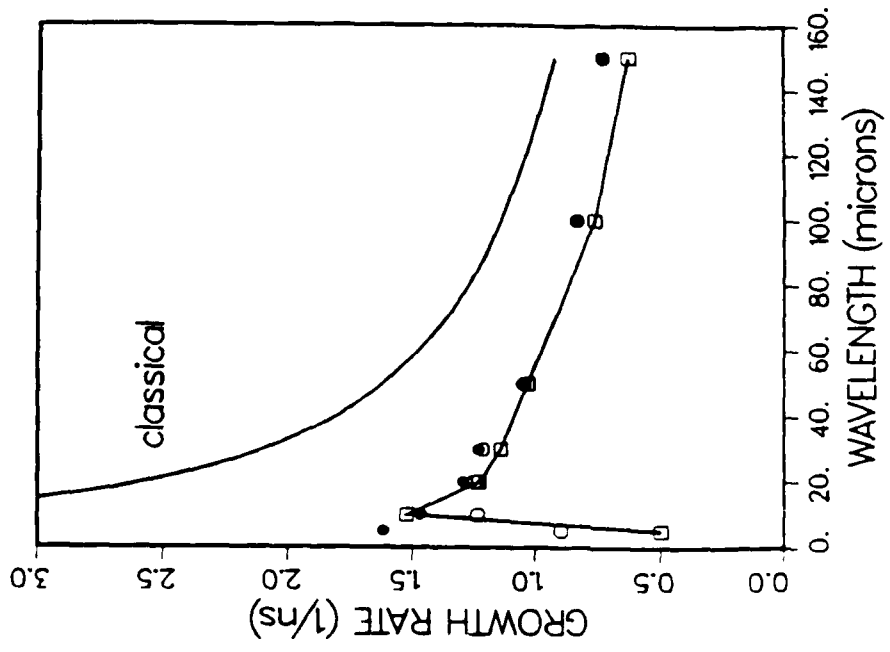
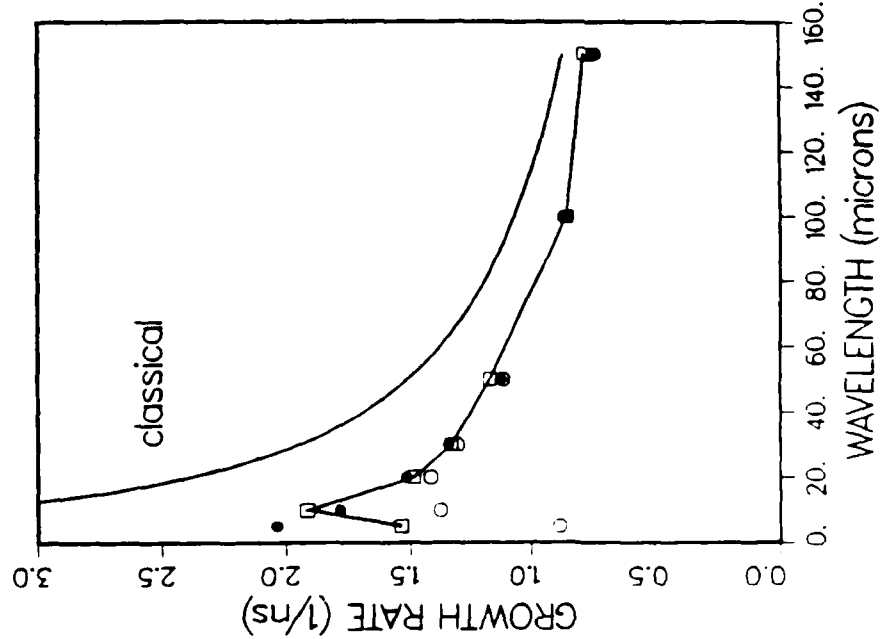


Fig. 2. Comparison of the classical growth rates (solid, curved line,  $(\text{kg})^{1/2}$ ) to the numerical growth rates (squares) as a function of perturbation wavelength for the  $1 \mu\text{m}$  laser light cases. Fig. 2a is for an initial target thickness of  $55 \mu\text{m}$  with an intensity of  $7 \times 10^{13} \text{ W/cm}^2$ . Fig. 2b is for an initial target thickness of  $150 \mu\text{m}$  with an intensity of  $3 \times 10^{14} \text{ W/cm}^2$ . Also shown are the theoretical growth rates (solid circles, Eq. IV-4) and modified theoretical growth rates, accounting for the finite thickness of the unstable layer (open circles); see Section IV. For Fig. 2a,  $V_a = 7 \times 10^5 \text{ cm/s}$  and  $h = 1.0 \mu\text{m}$ ; for Fig. 2b,  $V_a = 1.1 \times 10^6 \text{ cm/s}$  and  $h = 0.75 \mu\text{m}$ .



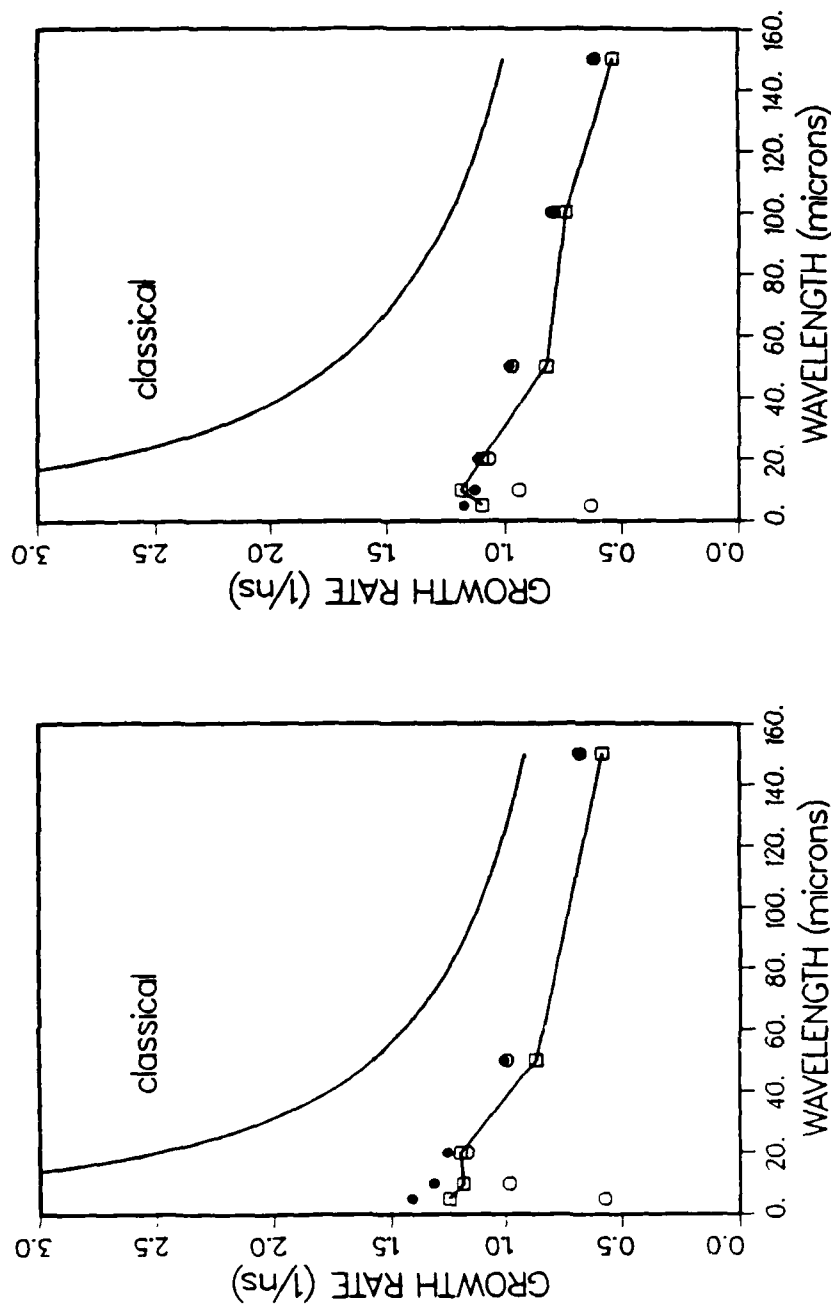


Fig. 3. Comparison of the classical growth rates (solid, curved line,  $(\text{kg})^{1/2}$ ) to the numerical growth rates (squares) as a function of perturbation wavelength for the  $1/2 \mu\text{m}$  laser light cases. Fig. 3a is for an initial target thickness of  $55 \mu\text{m}$  with an intensity of  $7 \times 10^{13} \text{ W/cm}^2$ . Fig. 3b is for an initial target thickness of  $150 \mu\text{m}$  with an intensity of  $3 \times 10^{14} \text{ W/cm}^2$ . Also shown are the theoretical growth rates (solid circles, Eq. IV-4) and modified theoretical growth rates, accounting for the finite thickness of the unstable layer (open circles); see Section IV. For Fig. 3a,  $V_a = 1.3 \times 10^6 \text{ cm/s}$  and  $h = 1.0 \mu\text{m}$ ; for Fig. 3b,  $V_a = 1.8 \times 10^6 \text{ cm/s}$  and  $h = 0.75 \mu\text{m}$ .

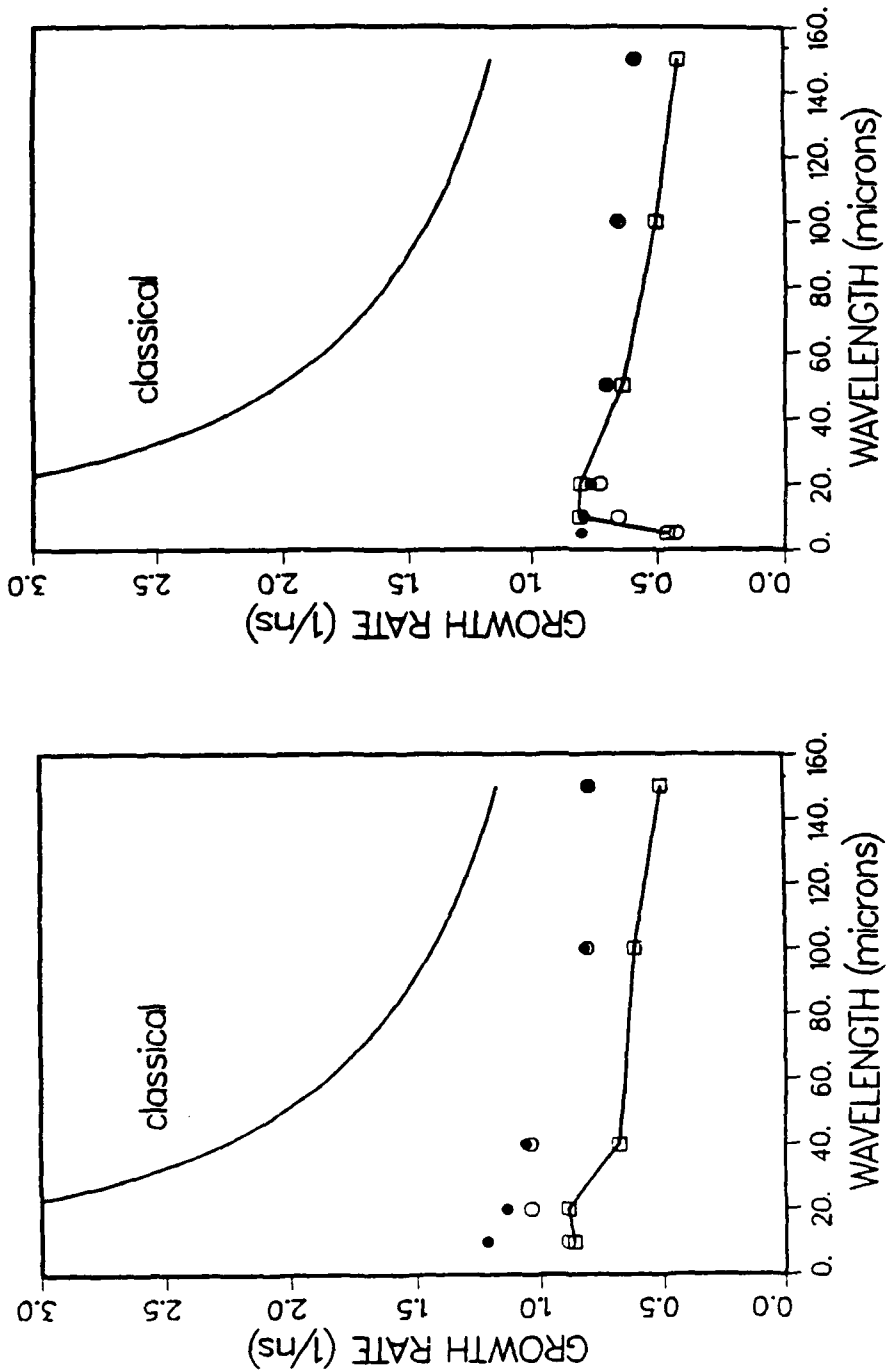


Fig. 4. Comparison of the classical growth rates (solid, curved line,  $(kg)^{1/2}$ ) to the numerical growth rates (squares) as a function of perturbation wavelength for the  $1/4 \mu m$  laser light cases. Fig. 4a is for an initial target thickness of  $55 \mu m$  with an intensity of  $7 \times 10^{13} W/cm^2$ . Fig. 4b is for an initial target thickness of  $150 \mu m$  with an intensity of  $3 \times 10^{14} W/cm^2$ . Also shown are the theoretical growth rates (solid circles) and modified theoretical growth rates, accounting for the finite thickness of the unstable layer (open circles); see Section IV. For Fig. 4a,  $V_a = 2.5 \times 10^6$  and  $h = 1.0 \mu m$ ; for Fig. 4b,  $V_a = 4 \times 10^6$  cm/s and  $h = 0.75 \mu m$ .

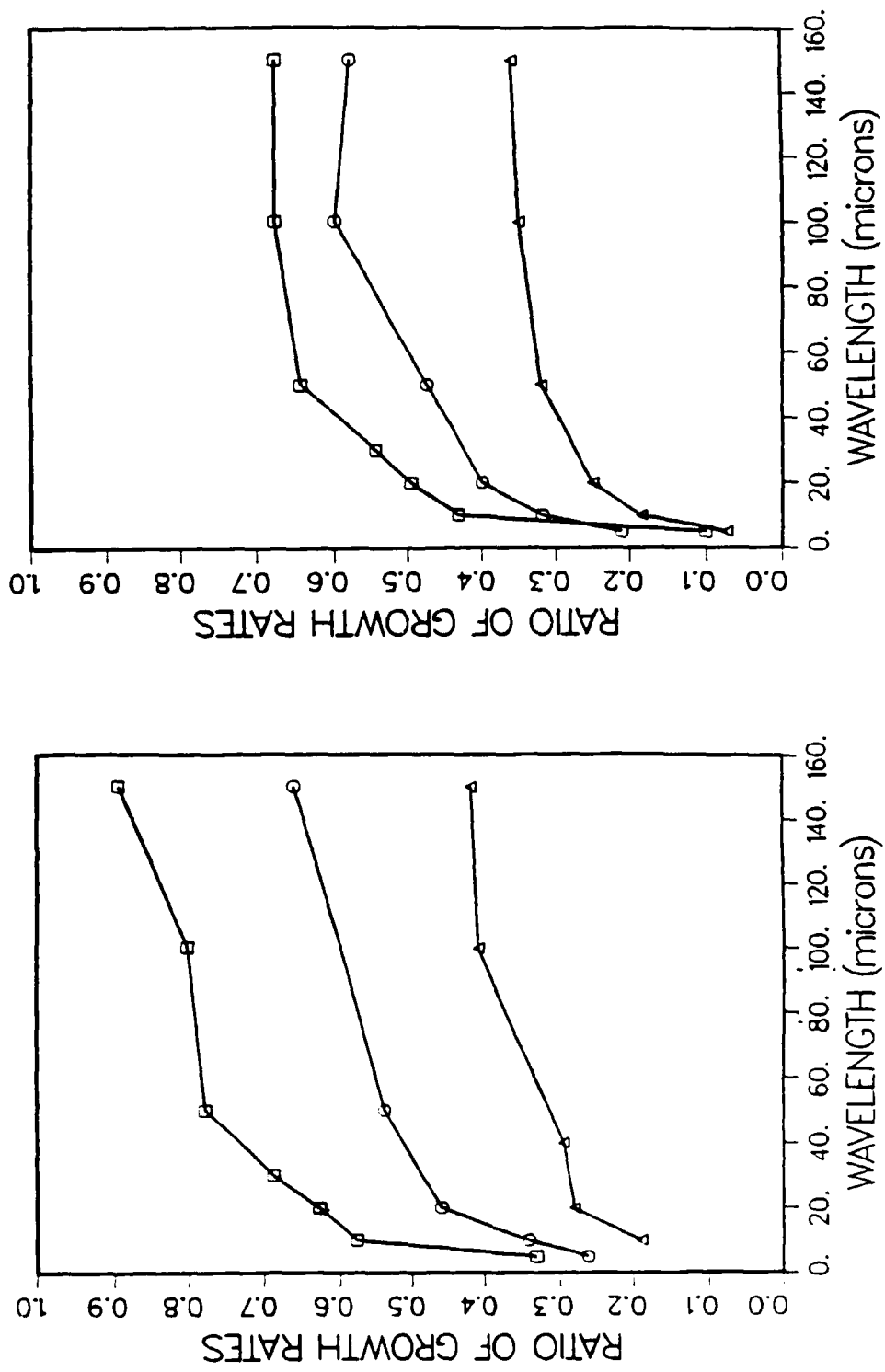


Fig. 5. The ratios of the numerical growth rates to the classical growth rates as a function of perturbation wavelength and laser wavelength. The triangle, circle and square symbols are for 1,  $1/2$  and  $1/4 \mu\text{m}$  laser light respectively. Fig. 5a is for an intensity of  $7 \times 10^{13} \text{ W/cm}^2$  and Fig. 5b is for an intensity of  $3 \times 10^{14} \text{ W/cm}^2$ .

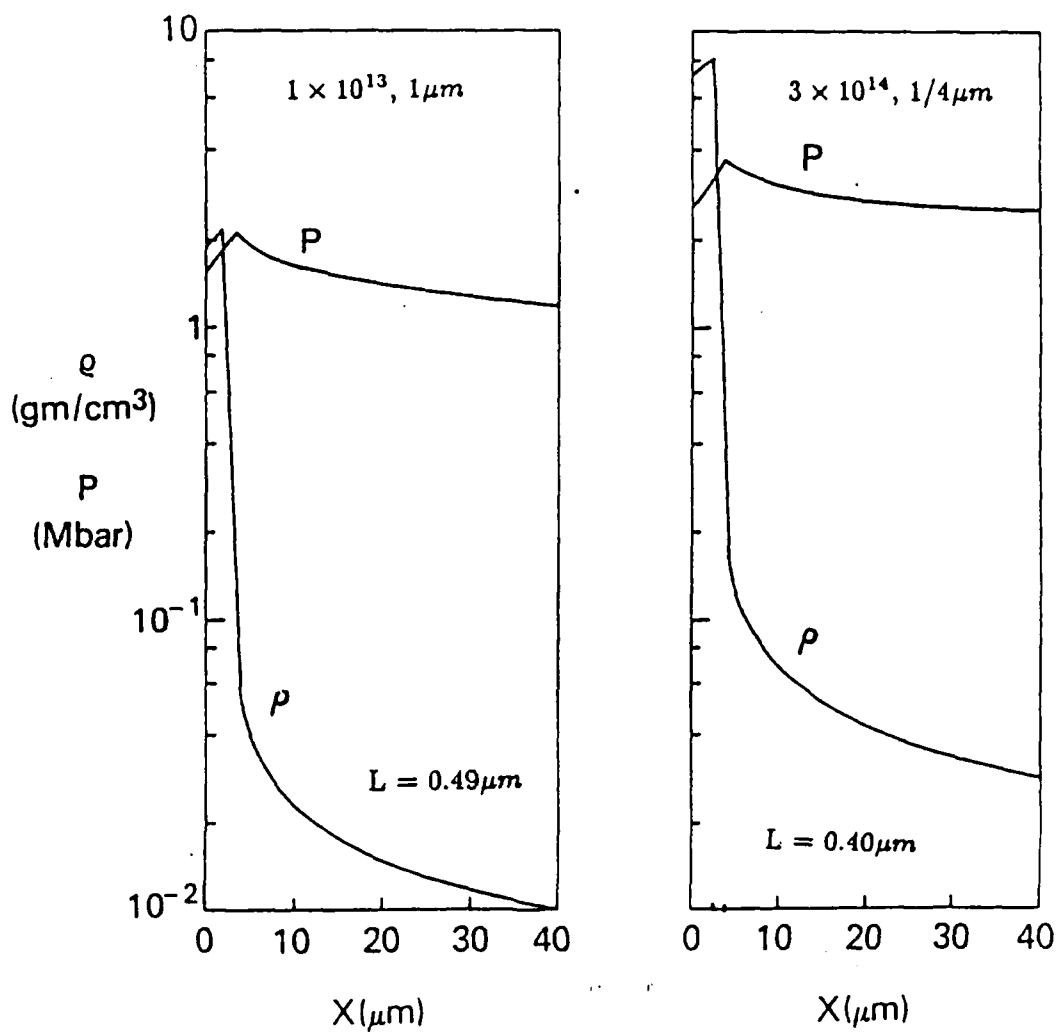


Fig. 6. One-dimensional density and pressure profiles for the cases (a)  $1 \mu\text{m}$ ,  $10^{13} \text{ W/cm}^2$  and (b)  $1/4 \mu\text{m}$ ,  $3 \times 10^{14} \text{ W/cm}^2$  under nearly steady-state conditions. The pressure in (b) is in units of 10 Mbar.

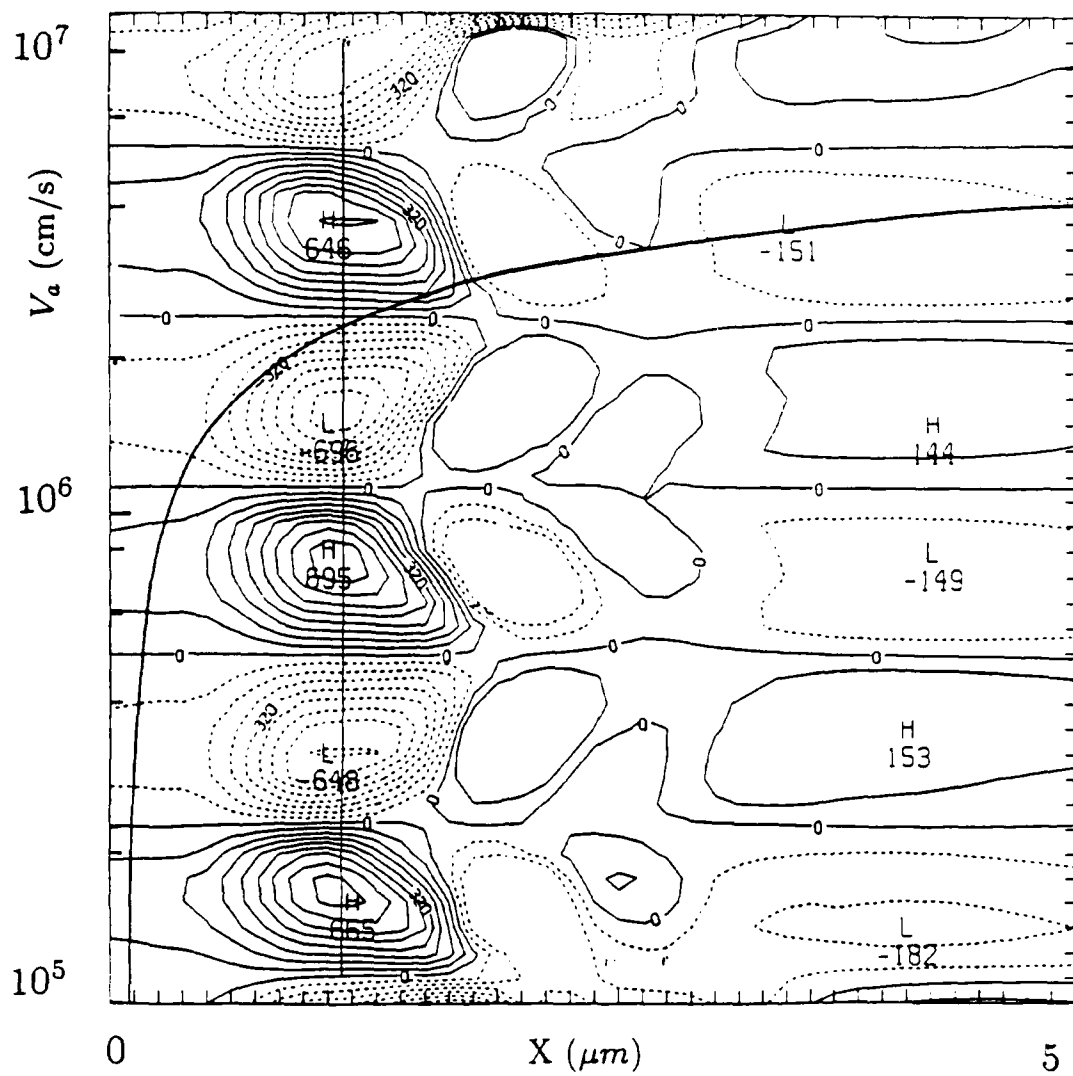


Fig.7. Isovorticity contours, in 12% increments of the maximum on the target surface early in the evolution of the  $20 \mu m$  RT instability with  $1/4 \mu m$ ,  $7 \times 10^{13} W/cm^2$  laser light. The laser is impinging the target from the right. The spatial dimensions are in microns. The dashed (solid) contours indicate clockwise (counterclockwise) flow. The ablation velocity ( $V_a$ , cm/s) is plotted on top of the vorticity contours. The solid vertical line illustrates the point at which the ablation velocity is measured.

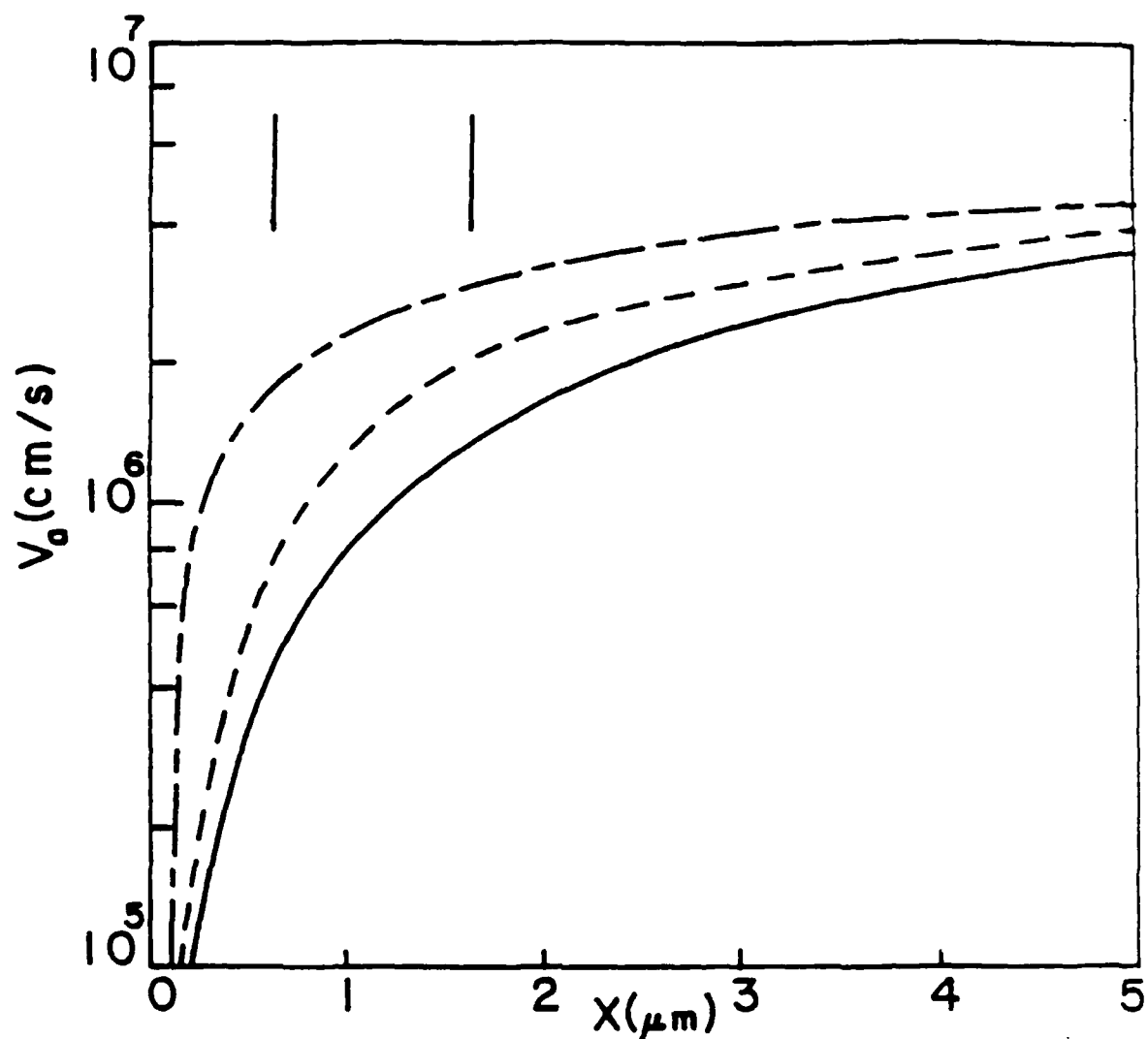


Fig.8. Ablation velocity ( $V_a$ ) as a function of distance from the target surface ( $X$ ) for 1 (solid), 1/2 (dashed) and 1/4 (dash-dotted)  $\mu\text{m}$  laser light at  $7 \times 10^{13} \text{ W/cm}^2$  under nearly steady-state conditions. The vertical lines approximately bracket the unstable vortex layer.

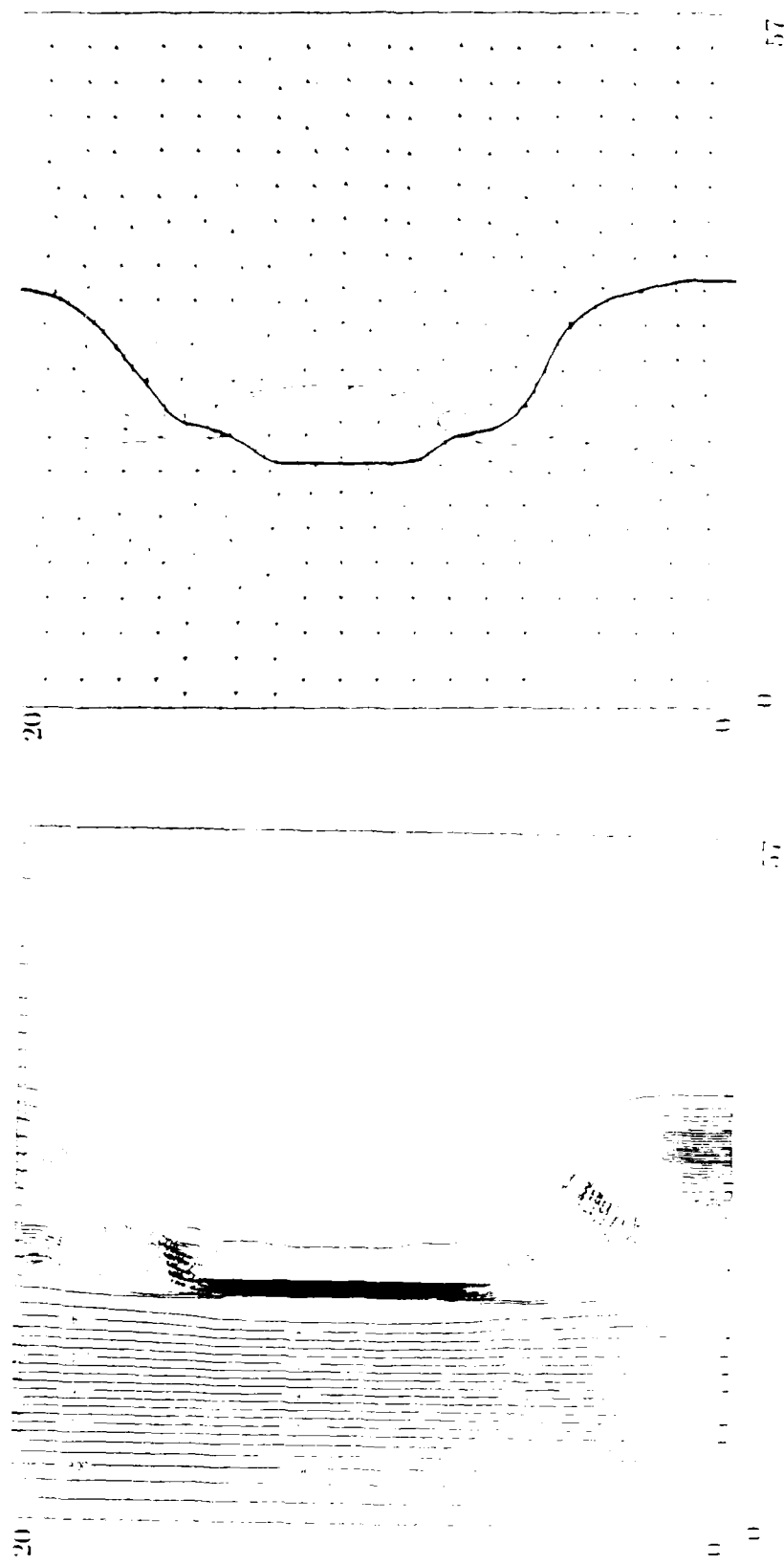


Fig. 9. Isodensity contours (a) and streamlines (b) after nearly 4  $e$ -foldings of RT growth for the  $20 \mu m$  perturbation wavelength with  $1/4 \mu m$  light at  $7 \times 10^{13} W/cm^2$ . The laser is impinging the target from the right. The dimensions are in microns and the time is 4 ns after the perturbation was imposed. The bold line in Fig. 12b delineates the  $0.20 \text{ gm}/\text{cm}^3$  density contour.

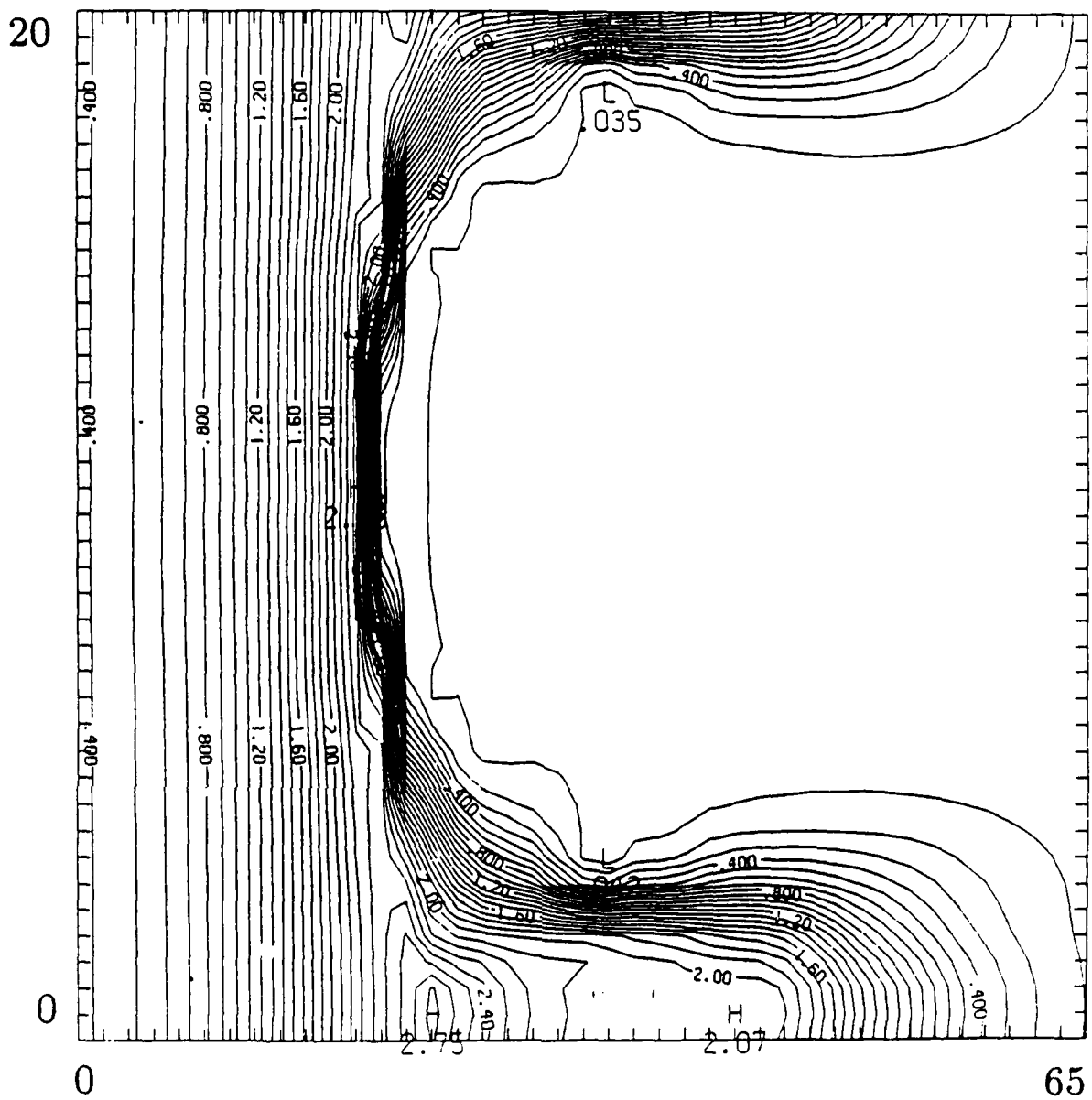


Fig. 10. Isodensity contours at 5 ns for the same conditions as in Fig. 12. This illustrates the typical nonlinear bubble-and-spike structure.

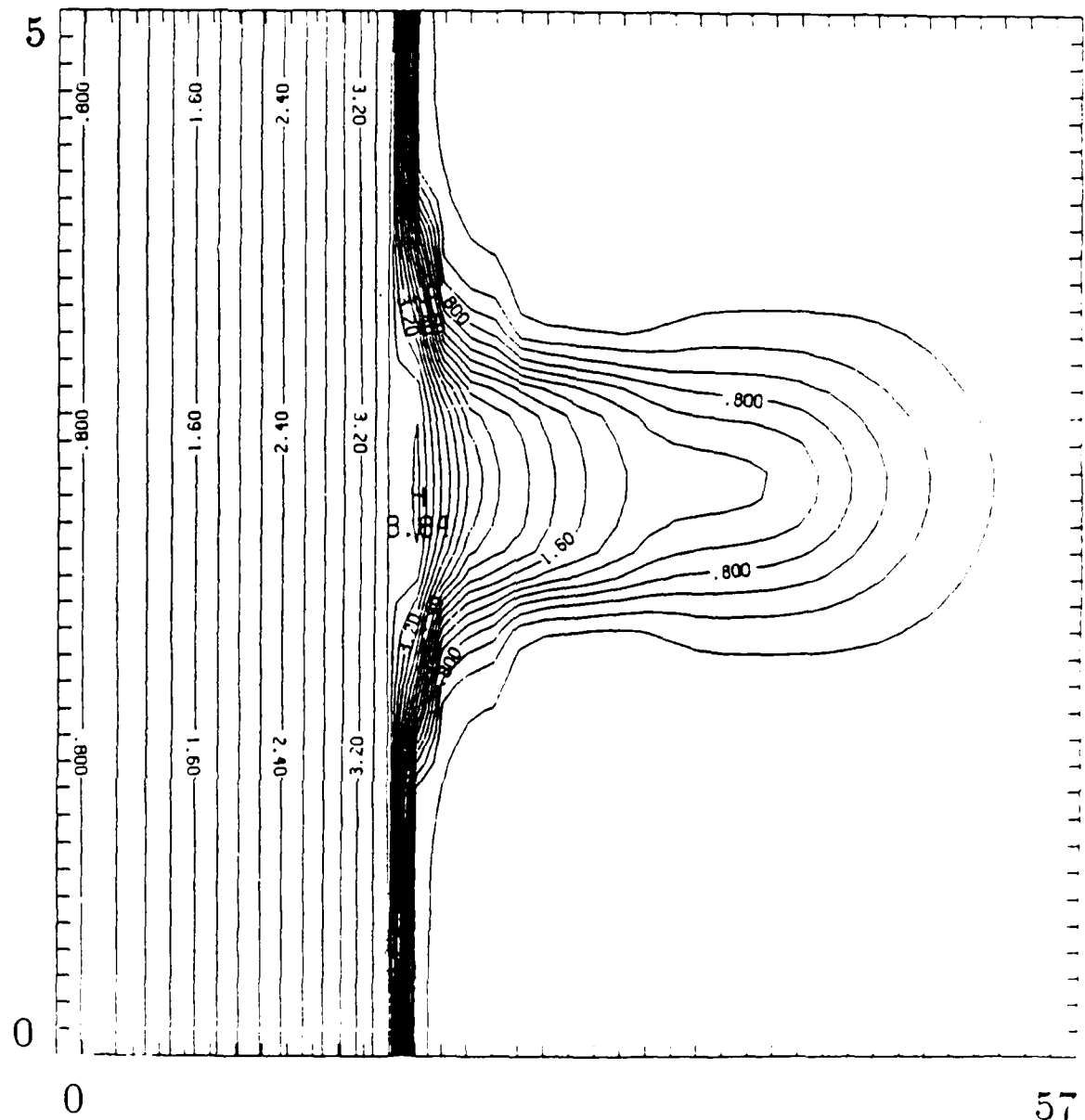
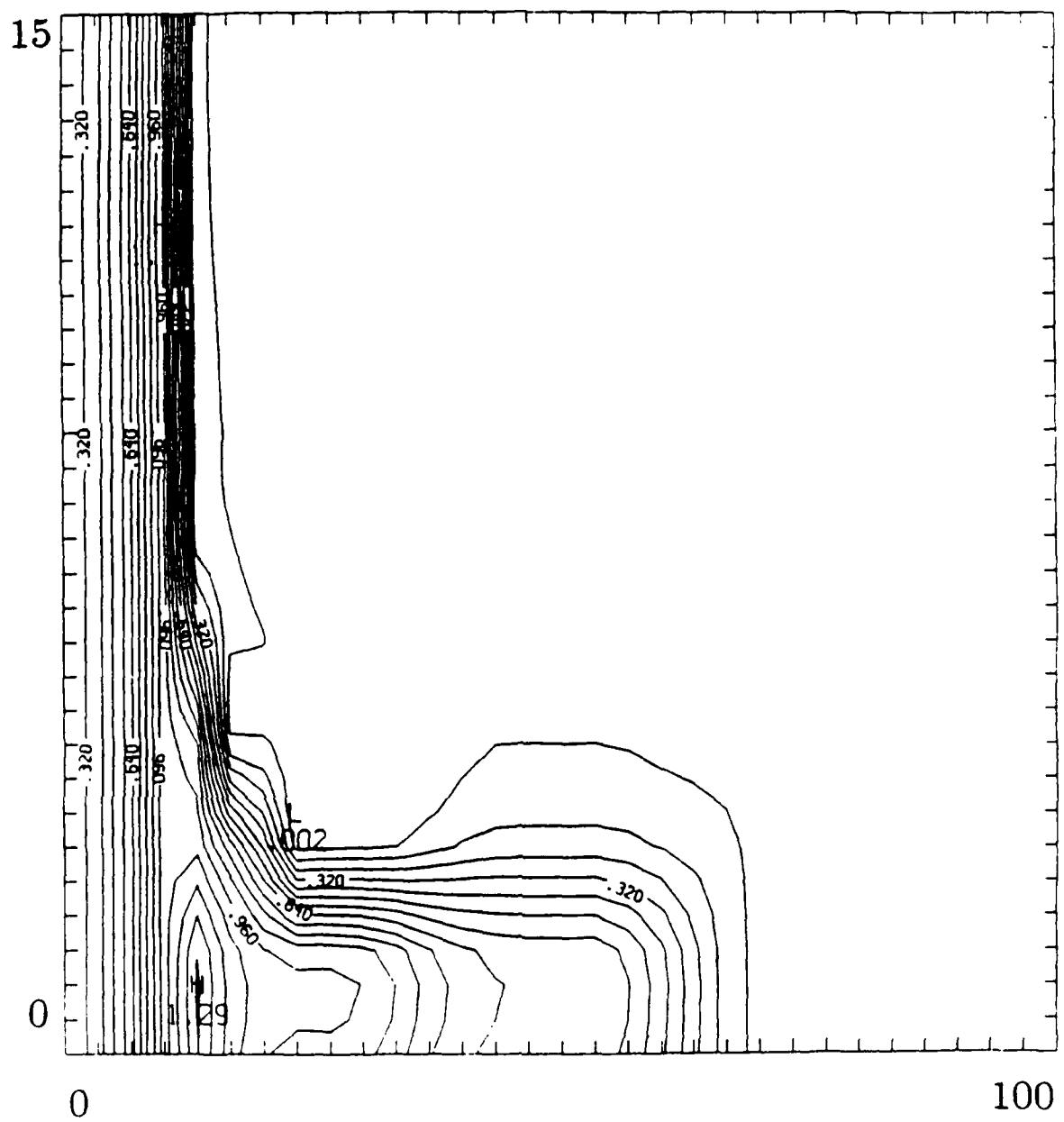


Fig.11. Isodensity contours illustrating the bubble-and-spike structure for a  $5 \mu\text{m}$  perturbation wavelength with  $1/2 \mu\text{m}$  laser light at  $7 \times 10^{13} \text{ W/cm}^2$ . The dimensions are in microns and the time is at 4.5 ns.



END

12 - 87

DTIC